

Computer Vision Methods for Fractographic Defect Detection in Titanium and Aluminum Alloys

Wasim Shebalny^a, Shifaa Khatib^a, Or Haim Anidjar^a, Mor Mega^b, and Tomer Weber^c

^aSchool of Computer Science , Ariel University, Ariel, Israel

^bThe Fracture and Fatigue Research Laboratory, Department of Mechanical Engineering and Mechatronics, Ariel University, Ariel, Israel

^cDepartment of Mechanical Engineering and Mechatronics, Ariel University, Ariel, Israel

Abstract

Additive manufacturing (AM) of titanium and aluminum alloys has emerged as a transformative technology in aerospace, biomedical, and energy applications, enabling the production of lightweight components with complex geometries. However, these alloys remain highly susceptible to fatigue failure, where microstructural defects accumulate and propagate into critical fractures. Understanding and quantifying this process is essential for improving material reliability. Traditional fractographic analysis relies on manual inspection of scanning electron microscopy (SEM) images, a procedure that is time-consuming, subjective, and difficult to standardize across specimens and laboratories.

In this work, we present a suite of computer vision methods designed to automate the detection and quantification of fatigue-induced defects in AM titanium and aluminum specimens. The approach integrates multi-scale contour analysis: external contours are extracted from specimen masks to define the overall geometry, while internal contours are detected for distinct crack-growth phases identified in fractographic heatmaps (dark red, red, yellow, cyan, blue). For each phase, binary masks and smoothed contours are generated, and their areas are computed in both pixel units and calibrated physical dimensions. Ellipse fitting is further applied as a geometric descriptor to characterize the progression of crack envelopes and the transition from fatigue to static fracture.

In addition to visual overlays, the methods automatically produce structured CSV files. These CSVs record per-specimen crack-zone areas (pixels and mm²) across all color phases, as well as aggregated statistics such as mean and standard deviation. This dual output—visual and numerical—provides a reproducible foundation for quantitative analysis and enables consistent comparisons across specimens. By combining contour-based analysis, geometric modeling, and automated data reporting, this work advances the development of standardized, computer vision-assisted fractography for additively manufactured metals.

1 Introduction

1.1 Additive Manufacturing (AM)

Additive manufacturing (AM) has become a transformative technology across aerospace, biomedical, automotive, and energy industries. Unlike conventional subtractive processes, AM fabricates components layer by layer, enabling lightweight geometries, complex designs, and efficient material use. Titanium and aluminum alloys are particularly attractive for AM due to their high strength-to-weight ratio, corrosion resistance, and biocompatibility. Despite these advantages, AM alloys often exhibit process-induced imperfections such as residual stresses, porosity, surface roughness, and microstructural inhomogeneity. These defects play a crucial role in determining the fatigue and fracture behavior of additively manufactured parts, thereby limiting their long-term reliability in safety-critical applications.

1.2 Fatigue Characteristics of Additively Manufactured Alloys

Fatigue is a dominant failure mode in structural alloys, and its characteristics are strongly affected by the manufacturing route. In traditional subtractive manufacturing (SM), components are produced from wrought or cast billets, typically resulting in well-controlled microstructures with relatively low porosity. Fatigue cracks in SM parts usually initiate at surface imperfections, inclusions, or machining marks, and their growth behavior is relatively well characterized.

In contrast, alloys produced by additive manufacturing (AM) often contain process-induced defects such as lack-of-fusion pores, unmelted particles, and surface roughness due to the layer-by-layer build strategy. Titanium and aluminum alloys fabricated by powder bed fusion or electron beam melting exhibit anisotropic microstructures, residual stresses, and localized heterogeneities that strongly influence crack initiation and propagation. As a result, fatigue performance in AM alloys is often inferior and less predictable compared to their SM counterparts.

Fractographic examination using scanning electron microscopy (SEM) has traditionally been employed to identify fatigue striations, crack origins, and transition zones. While effective, this manual inspection is labor-intensive, requires expert knowledge, and suffers from subjectivity, making it difficult to achieve reproducibility across laboratories. With the growing adoption of AM, there is a pressing need for quantitative, automated approaches to characterize fatigue cracks and fracture surfaces in order to improve predictive models and ensure structural integrity.

1.3 Computer Vision and Machine Learning in Additive Manufacturing

In recent years, computer vision (CV) and machine learning (ML) have gained prominence in additive manufacturing research, addressing challenges in both in-situ monitoring and post-mortem analysis. CV algorithms have been applied to detect pores, inclusions, and surface defects directly from optical or SEM images, while ML methods such as convolutional neural networks (CNNs) and U-Net architectures have shown promise in segmentation tasks for microstructural features. These data-driven approaches can accelerate defect detection and support predictive maintenance of AM parts. However, most ML-based methods require extensive annotated datasets and significant computational resources, limiting their applicability in small-scale or highly specialized studies. In contrast, contour-based computer vision techniques offer a lightweight and interpretable alternative. By focusing on the geometric properties of crack zones and their progression, such methods can provide reproducible quantitative measurements without the need for large-scale training. This study builds upon this paradigm by developing a contour- and geometry-driven framework for automated fatigue fracture analysis of AM titanium and aluminum alloys.

1.4 Our contribution

This study contributes a reproducible and geometry-driven framework for fatigue crack characterization in additively manufactured titanium and aluminum alloys. In contrast to traditional manual fractographic inspection, our approach introduces a fully automated image analysis pipeline based on contour extraction and geometric modeling.

First, we implement a multi-phase segmentation strategy using color-encoded heatmaps derived from post-mortem fractographic images. These heatmaps, typically annotated in five distinct color bands (dark red, red, yellow, cyan, and blue), correspond to successive stages of crack growth. From these, we extract both external specimen boundaries and internal crack contours, generating binary masks and smoothed geometric representations for each phase.

Second, we calibrate the contour areas using a fixed pixel-to-micron ratio, enabling quantification of crack zone dimensions in both pixel and physical units. To model crack propagation envelopes and transitions between fatigue and static fracture, we apply ellipse fitting as a shape descriptor for each segmented region.

Finally, the analysis pipeline outputs structured CSV files for each category of specimens, recording the area of each crack-growth phase and aggregating key statistics such as mean and standard deviation.

To the best of our knowledge, this work represents one of the first domain-specific integrations of multi-phase heatmap analysis, geometric modeling, and data reporting in post-mortem fracture evaluation of AM metals.

2 Dataset

The experimental dataset used in this study consists of scanning electron microscopy (SEM) images of fracture surfaces from titanium and aluminum alloys fabricated by additive manufacturing processes. These specimens represent different processing routes and alloy categories, providing a diverse basis for evaluating our computer vision framework. The dataset can be divided into three groups:

2.1 SLM Ti-6Al-4V

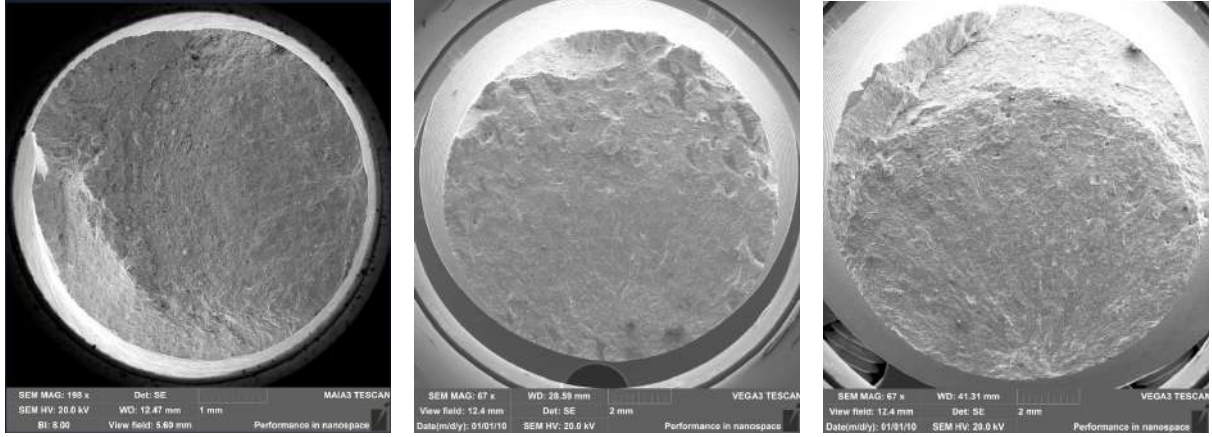
Selective Laser Melting (SLM) is a powder bed fusion technique that employs a high-power laser to selectively melt metal powder in a layer-by-layer fashion. Ti-6Al-4V produced by SLM is widely used in aerospace and biomedical applications due to its high specific strength and biocompatibility. However, the rapid solidification rates and complex thermal cycles inherent to SLM often result in microstructural heterogeneity, anisotropy, and process-induced defects such as porosity or unmelted particles. These features strongly influence fatigue crack initiation and growth. The SEM images collected for this category capture post-mortem fracture surfaces where such defects act as crack nucleation sites.

2.2 EBM Ti-6Al-4V

Electron Beam Melting (EBM) is another powder bed fusion process, in which an electron beam is used to melt the powder under vacuum conditions. Compared to SLM, EBM generally produces coarser microstructures due to slower cooling rates, but it also reduces residual stresses because of the high preheat temperatures applied during processing. Ti-6Al-4V produced by EBM is increasingly used for structural and medical implant applications. In our dataset, SEM images from EBM specimens highlight the influence of microstructural morphology and defect distribution on fatigue fracture characteristics, offering a contrast to the SLM counterparts.

2.3 Aluminum Alloys (SEM Imaging)

In addition to titanium alloys, our dataset includes SEM images of aluminum alloys fabricated by additive manufacturing. Aluminum alloys are of great interest for lightweight structural components in automotive and aerospace sectors. However, their relatively high susceptibility to porosity, oxide inclusions, and solidification defects poses challenges for fatigue performance. The SEM images collected for these specimens capture fracture surfaces with characteristic features such as dimples, void coalescence, and microcrack networks. These aluminum datasets provide an additional validation platform for our contour-based defect detection methods.



(a) SLM Ti-6Al-4V specimen

(b) EBM Ti-6Al-4V specimen

(c) Aluminum alloy specimen

Figure 1: Representative SEM fracture surface images from the dataset: (a) SLM Ti-6Al-4V, (b) EBM Ti-6Al-4V, (c) Aluminum alloy.

3 Preprocessing

Before applying our computer vision methods, all dataset images underwent a standardized preprocessing pipeline to ensure consistency and compatibility across specimens. The raw images were obtained from scanning electron microscopy (SEM) in TIFF format, with varying resolutions and aspect ratios. Two main preprocessing steps were applied: format conversion and spatial normalization.

3.1 Format Conversion

The original SEM images were stored in `.tif` format, which can pose compatibility issues with certain computer vision libraries. To facilitate downstream processing, all images were batch-converted to the more widely supported `.png` format using the `PIL` (Python Imaging Library). This conversion preserved the image quality while providing a standardized format for subsequent contour extraction and analysis.

3.2 Cropping and Normalization

SEM images often contain non-square dimensions, which complicates certain geometric analyses and visualization tasks. To normalize the dataset, each image was converted to grayscale in order to determine its dimensions. The smaller side (width) was then used to crop the image into a centered square region of interest. This ensured that all images shared a consistent aspect ratio and eliminated unnecessary background regions.

After cropping, the original image files were replaced with the preprocessed versions in the dataset directory, creating a uniform collection of square, `.png`-formatted SEM images ready for segmentation and contour extraction.

Through this preprocessing pipeline, we established a reproducible baseline for image preparation. The resulting dataset consists exclusively of square, high-resolution SEM images in `.png` format, enabling reliable downstream analysis of crack-growth phases and fatigue features across different alloy categories.

4 Related Work

The integration of computer vision into fracture mechanics has undergone substantial development in recent years, particularly with the increasing availability of high-resolution scanning electron microscopy (SEM) images of metallic alloys. Traditionally, fractographic studies relied on expert-driven visual inspection to classify features such as dimples, cleavage facets, and fatigue striations [15, 1]. While this approach has produced decades of valuable insights into failure mechanisms, it is inherently limited by its subjectivity, labor intensity, and the difficulty of establishing reproducible quantitative metrics across laboratories.

Early computational methods in fractography emphasized image processing techniques rather than full computer vision or machine learning frameworks. Researchers applied spatial domain methods such as texture analysis, gray-level co-occurrence matrices (GLCM), and fractal analysis to SEM images in order to quantify surface roughness and morphological features [25]. These methods were often combined with transform domain approaches—Fourier, wavelet, or Gabor transforms—to enhance contrast and highlight characteristic features of crack propagation. Edge detection and peak-tracking algorithms were also employed to identify fatigue striations and crack progression marks [33, 15]. While effective at enhancing qualitative interpretation, such techniques often demanded significant manual supervision, which limited their scalability and robustness in complex fracture surfaces typical of additively manufactured alloys.

The last decade has witnessed a growing adoption of machine learning (ML) and artificial intelligence (AI) in materials characterization, including fractography. Neural networks, support vector machines (SVMs), and random forests have been employed to classify fracture types, yielding improved accuracy compared to handcrafted approaches [7, 28]. Convolutional neural networks (CNNs) and their encoder–decoder variants such as U-Net have shown notable success in segmenting SEM images of microstructures [14]. In one study, a U-Net architecture achieved more than 80% Dice score accuracy in distinguishing intergranular from transgranular fractures, substantially outperforming classical thresholding and watershed methods [14]. Similarly, CNN-based classifiers have demonstrated the ability to identify fatigue dimples and cleavage facets with higher consistency than manual labeling, albeit at the cost of requiring large annotated datasets and significant computational resources [33, 31, 28]. A recent study further confirmed the potential of deep learning in this field, showing that the integration of image processing and CNN-based models yields promising results for fatigue and failure analysis of titanium alloys in additive manufacturing [3].

A prominent trend in recent literature is the fusion of traditional feature-extraction methods with modern AI architectures. Techniques such as Local Binary Patterns (LBP) and Histogram of Oriented Gradients (HOG) have been integrated with linear discriminant analysis (LDA) or SVMs to classify brittle versus ductile fractures with reported accuracies exceeding 90% [28, 7]. More recent approaches have extended this fusion to object detection frameworks: by combining handcrafted features with YOLO-based detection networks, crack localization and phase classification have been achieved with F1 scores above 90%, particularly in concrete and metallic structural systems [31]. These hybrid pipelines demonstrate the utility of preprocessing and feature engineering as performance multipliers even in deep learning environments.

Despite these advances, significant challenges remain for automated fractography of additively manufactured alloys. AM alloys introduce unique complexities such as process-induced porosity, lack-of-fusion defects, and anisotropic microstructures, which are poorly represented in many existing datasets [20, 6, 23, 12]. Moreover, while deep learning approaches have achieved high accuracy [14, 33, 3], their reliance on large annotated datasets, limited interpretability, and lack of standardized evaluation frameworks restricts their adoption in specialized domains such as failure analysis. Reproducibility across laboratories is still lacking, as most studies emphasize accuracy on small datasets without robust calibration [27, 9].

Our study addresses these gaps by advancing a lightweight, interpretable, and geometry-driven framework for fatigue fractography of AM titanium and aluminum alloys. In contrast to prior ML-

heavy approaches, we employ contour extraction, multi-phase heatmap segmentation, and ellipse fitting as physically interpretable descriptors of crack propagation. This methodology enables reproducible quantitative reporting across specimens without the need for massive annotated datasets, thereby complementing data-driven methods and providing a standardized alternative for comparative analysis.

5 Proposed approach

In this section, we present the pipeline developed for automated fractographic analysis of additively manufactured Ti-6Al and Al alloys. The workflow proceeds through a sequence of stages, from preprocessing and inner-shape extraction to phase-specific contour detection and quantitative reporting. Each stage is described below.

5.1 Inner-Shape Extraction

The objective of this stage was to isolate the specimen geometry from SEM images, producing a clean binary mask and corresponding segmented region of interest. This procedure ensures that all subsequent crack-phase analyses are restricted to the physically relevant specimen area. The extraction was carried out in three phases, illustrated in Figure ??.

Phase I: Mask generation. First, local contrast was enhanced using Contrast-Limited Adaptive Histogram Equalization (CLAHE). Unlike global histogram equalization, CLAHE operates on small tiles and prevents over-amplification of noise in homogeneous regions, which is especially important for SEM images where grayscale variations are subtle. The enhanced image was then smoothed using a Gaussian filter, reducing high-frequency noise that might otherwise produce fragmented edges. Edge detection was performed with the Canny operator, using adaptive thresholds derived from image intensity statistics. This approach improves robustness across specimens by adapting to different brightness and contrast levels. The resulting edge maps were dilated to strengthen weak edges and closed morphologically to ensure continuity of the specimen boundary.

Phase II: Contour detection. From the binary edge maps, contours were identified using the `findContours` operation in OpenCV. To suppress irrelevant objects and small artifacts, a minimum-area threshold was applied. The largest contour was retained as the candidate specimen outline. In cases where the specimen boundary showed irregularities or fringe noise, a circular constraint was added: the contour was intersected with a circular mask centered on the specimen, effectively discarding peripheral artifacts without altering the global geometry.

Phase III: Mask refinement and segmentation. The contour was rasterized into a binary mask, which was further refined by morphological opening (removing small isolated foreground pixels) and closing (filling small holes inside the specimen region). This sequence of operations preserves the overall shape while removing high-frequency noise. Finally, the refined mask was applied to the SEM image to generate the segmented inner shape. This segmented region serves as the reference domain for all subsequent crack-phase analyses.

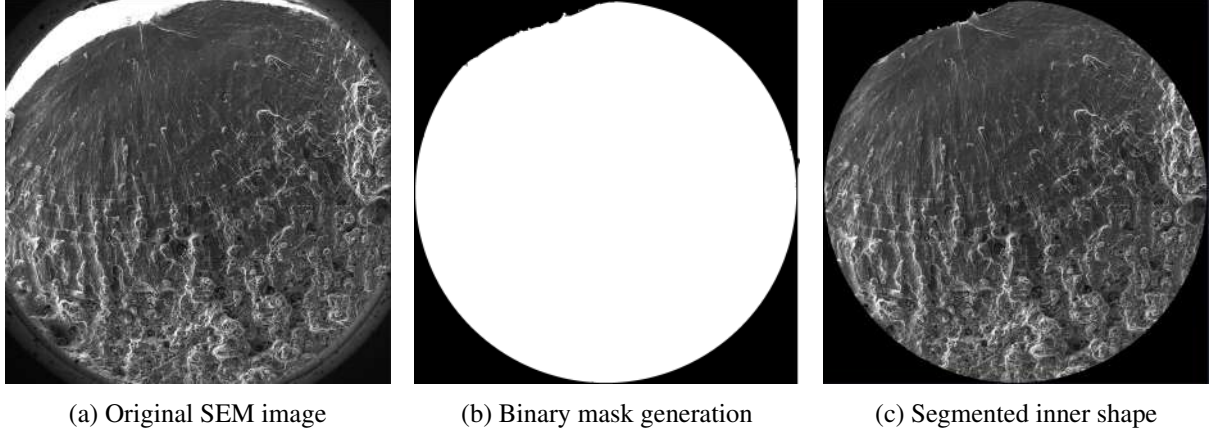


Figure 2: Example of inner-shape extraction

5.2 Heatmap Generation

Following the segmentation of the specimen’s inner contour, the next stage of our pipeline was dedicated to enhancing image details for secondary analysis by generating heatmaps. This stage is crucial for amplifying fracture-related features that are often difficult to observe directly in raw SEM images. The resulting heatmaps improve interpretability, facilitate anomaly detection, and provide the quantitative foundation for subsequent crack-phase contour analysis.

Motivation. While raw SEM images provide high-resolution information, their grayscale contrast often fails to reveal subtle fatigue cracks and microstructural irregularities. By transforming the segmented images into gradient-based heatmaps, we enhance the visibility of structural transitions, enabling both qualitative visualization and quantitative measurement of fracture zones. Heatmaps also provide a standardized representation, ensuring consistency across specimens.

Enhancement and gradient magnitude. The process begins with grayscale conversion of the segmented specimen, which standardizes intensity values between 0 (black) and 255 (white). To suppress high-frequency noise, the grayscale image is smoothed using a Gaussian kernel. This ensures that subsequent edge detection highlights only meaningful discontinuities in surface structure. The Sobel operator is then applied in the horizontal and vertical directions to approximate image gradients. The gradient magnitude at each pixel is computed as

$$M(x, y) = \sqrt{G_x(x, y)^2 + G_y(x, y)^2},$$

where G_x and G_y denote the intensity derivatives in the x and y directions, respectively. This operation highlights edges and discontinuities that are associated with crack propagation and phase boundaries. Although Sobel edges are inherently thicker than those detected by other operators, the method offers a favorable balance between computational efficiency and robustness.

Sliding window aggregation. Relying solely on pixel-wise gradient responses can lead to noisy or fragmented heatmaps, particularly in regions of low signal-to-noise ratio. To address this, a sliding window technique is employed to aggregate local gradient information over small neighborhoods. For each $n \times n$ window, the average response is computed as

$$G = \frac{1}{n^2} \sum_{i=1}^n \sum_{j=1}^n I_{i,j}^2,$$

where $I_{i,j}$ represents the gradient intensity at position (i, j) . In our implementation, a window size of 201×201 pixels with a stride of 10 pixels was selected, balancing resolution with computational

efficiency. This operation smooths isolated fluctuations while emphasizing regional fracture patterns, thereby improving detection accuracy along crack edges. Such regional aggregation has been shown in recent studies to enhance crack-edge detection in metallic alloys.

Contrast normalization and visualization. To further enhance the clarity of structural details, the aggregated gradient magnitude map is processed with histogram equalization, redistributing intensity values evenly across the dynamic range. This increases global contrast and ensures that both weak and strong features are equally represented. The equalized gradient map is then transformed into a pseudo-colored heatmap using the JET colormap. In this representation, low gradient magnitudes are mapped to blue, intermediate values to green, and high magnitudes to red, effectively highlighting zones of high structural activity. To avoid background interference, all pixels outside the segmented mask are set to black. The final heatmaps thus provide an intuitive and high-contrast visualization of fracture features.

Stepwise process. The transition from the segmented SEM image to the final heatmap can be described in the following steps, where each filtering or enhancement technique is detailed:

1. **Original segmented SEM image (A):** The process begins with the cropped and masked specimen image obtained from the inner-shape extraction stage. This ensures that only the physically relevant specimen area is considered for analysis.
2. **Grayscale conversion (B):** The RGB SEM image is converted into grayscale, mapping intensities to the range $[0, 255]$. This simplifies processing by reducing dimensionality while preserving structural information. Grayscale representation is sufficient since crack edges and microstructural features are intensity-based rather than color-based.
3. **Gaussian blurring (C):** A Gaussian filter with kernel size (13×13) is applied to the grayscale image. The Gaussian filter performs a weighted average of neighboring pixels, with weights decreasing as distance from the center increases. This reduces high-frequency noise, ensuring that only prominent structural changes are highlighted in subsequent edge detection.
4. **Sobel operator – X direction (D):** The Sobel operator is applied in the horizontal direction to compute G_x , emphasizing vertical edges. This convolution uses the discrete kernel

$$K_x = \begin{bmatrix} -1 & 0 & 1 \\ -2 & 0 & 2 \\ -1 & 0 & 1 \end{bmatrix},$$

which calculates the intensity gradient along the x -axis.

5. **Sobel operator – Y direction (E):** Similarly, the Sobel operator is applied in the vertical direction to compute G_y , emphasizing horizontal edges, using the kernel

$$K_y = \begin{bmatrix} -1 & -2 & -1 \\ 0 & 0 & 0 \\ 1 & 2 & 1 \end{bmatrix}.$$

6. **Combined gradient magnitude (F):** The overall edge strength is computed by combining G_x and G_y according to

$$M(x, y) = \sqrt{G_x(x, y)^2 + G_y(x, y)^2},$$

producing a gradient magnitude map. This map highlights intensity discontinuities that correspond to crack boundaries and fracture-related features.

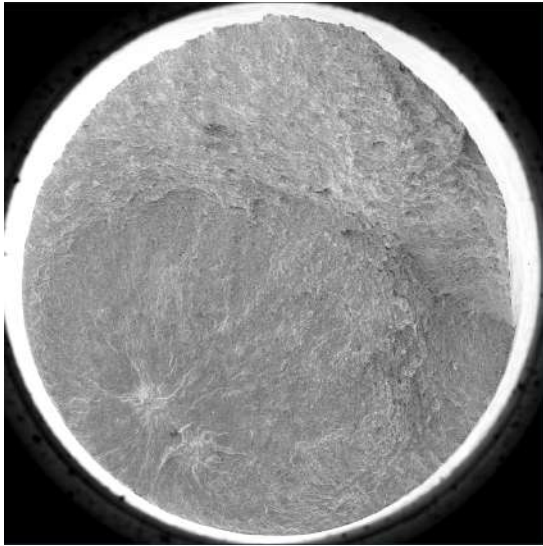
7. **Sliding window averaging (G):** A localized averaging technique is applied to smooth the gradient magnitude map and reduce sensitivity to noise. For each window of $n \times n$ pixels (here 201×201), the aggregated gradient response is computed as

$$G = \frac{1}{n^2} \sum_{i=1}^n \sum_{j=1}^n I_{i,j}^2,$$

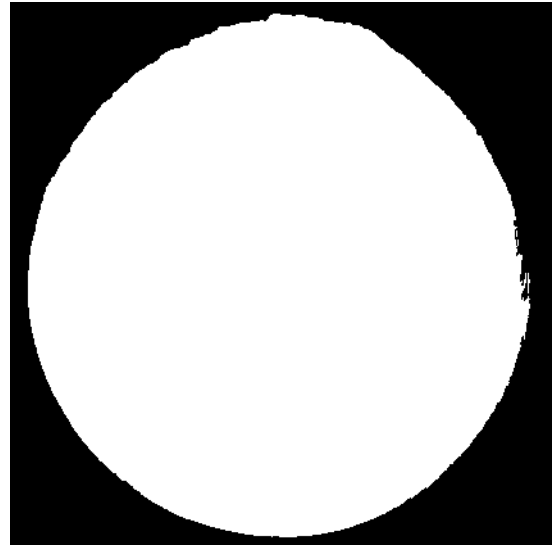
where $I_{i,j}$ is the intensity of pixel (i, j) . This sliding window (stride = 10 pixels) produces a heat distribution that emphasizes regional crack activity rather than isolated pixel responses.

8. **Histogram equalization (H):** The aggregated gradient map is equalized so that pixel intensities are spread more evenly across the full range [0,255]. This enhances the visibility of both weak and strong features, improving global contrast.
9. **Final pseudo-colored heatmap (I):** The equalized gradient map is mapped into a pseudo-color domain using the JET colormap. Blue corresponds to low gradient intensity (stable regions), green to moderate intensity, and red to high intensity (potential crack initiation/propagation sites). Background pixels outside the specimen mask are set to black, ensuring that only specimen features are visualized.

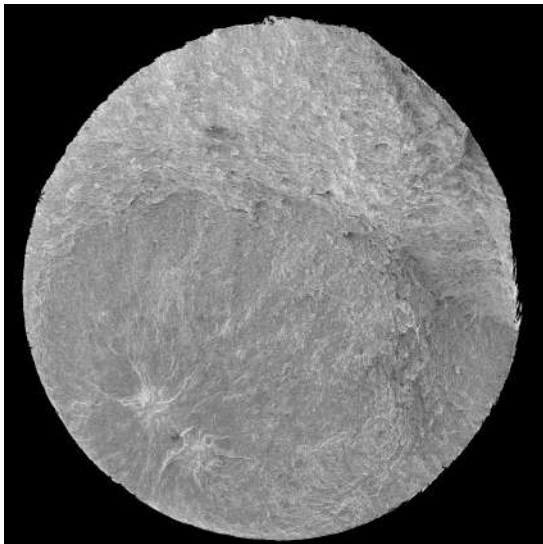
Outcome. The resulting heatmaps highlight the intensity and distribution of fracture features across the specimen surface. Warm-colored regions (red, yellow) correspond to areas of higher gradient activity and potential crack initiation or propagation, while cool-colored regions (blue, green) represent more stable zones. These enhanced visualizations enable a reproducible and systematic analysis of crack-growth phases, which is essential for standardized fractographic studies.



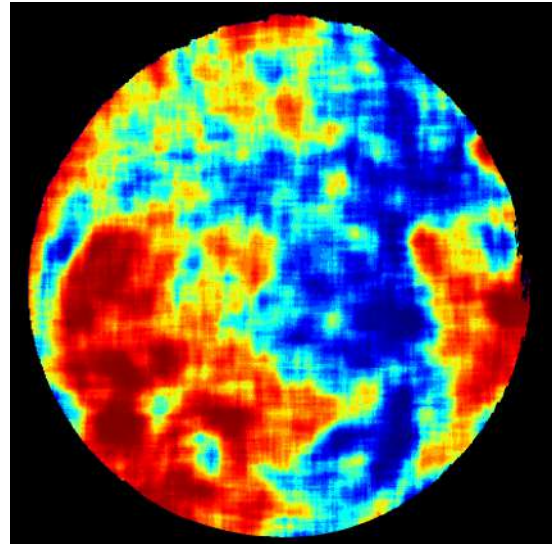
(a) Original SEM input



(b) Binary mask extracted from contours



(c) Segmented specimen obtained by applying the mask



(d) Final colored heatmap emphasizing fracture-related regions

Figure 3: Pipeline steps for heatmap generation: (a) original SEM image, (b) binary mask, (c) segmentation output, (d) final heatmap.

6 Methodology for Automated Crack Zone Delineation

The critical step following heatmap generation is the automated identification and delineation of the primary crack zone. This process translates the qualitative, colour-coded visualisation into a quantitatively defined region of interest. To achieve this with both precision and robustness, our pipeline integrates a dual-method approach, leveraging specific functions from the OpenCV (`cv2`) and SciPy libraries to perform colour segmentation, geometric filtering, and shape approximation.

6.1 Primary Method: Spatially-Constrained Contour Filtering

Our primary method is designed to precisely identify the crack's epicentre by analyzing the spatial relationship between colour-coded regions of the heatmap.

6.1.1 Colour Segmentation in HSV Space

The analysis begins by converting the heatmap from the BGR colour space to HSV (Hue, Saturation, Value) using the `cv2.cvtColor` function. This transformation is crucial as the HSV model isolates colour (hue) from brightness (value), allowing for more reliable segmentation under varying illumination conditions than the interdependent RGB channels. Using predefined thresholds, binary masks are generated for key colour regions with the `cv2.inRange` function. This creates distinct masks for the broader high-stress area (dark red and red hues) and the localised zones of peak intensity (orange hues). To refine these masks, noise and minor artifacts are removed through morphological transformations executed by `cv2.morphologyEx`, ensuring that only significant regions are considered.

6.1.2 Centroid-Inclusion Logic

The core of this method is a geometric filtering step that identifies the most probable crack zone. First, contours are extracted from the orange mask using `cv2.findContours`. For each detected orange contour, its geometric centroid is calculated from its image moments, which are computed using the `cv2.moments` function. The algorithm then programmatically checks if this centroid lies within the boundary of any contour from the red mask. This spatial test is performed using the `cv2.pointPolygonTest` function, which returns a positive value if the point is inside the contour. This logic enforces a key physical assumption: that the most critical fracture activity (orange) is spatially nested within a larger region of high stress (red). The largest-area orange contour that satisfies this condition is selected as the definitive crack zone. Illustration could be seen in Figure 4.

6.2 Alternative Method: Convex Hull Approximation

For specimens where the primary crack zone is highly fragmented or forms a complex, non-convex shape, a robust fallback method is employed to ensure a reliable boundary is always found.

Shape Approximation with Convex Hull This approach first combines the red and orange masks to create a single, unified region representing all significant fracture activity. After finding the largest contour in this consolidated mask, its vertices are passed to the `scipy.spatial.ConvexHull` function. This function computes the smallest possible convex polygon that encloses all points of the contour, effectively creating a "shrink-wrapped" boundary around the entire region. This convex hull provides a simplified, robust approximation of the fracture zone's extent. While it may slightly overestimate the area compared to a tight-fitting contour, it guarantees a single, closed boundary for irregularly shaped regions where the primary method might fail.

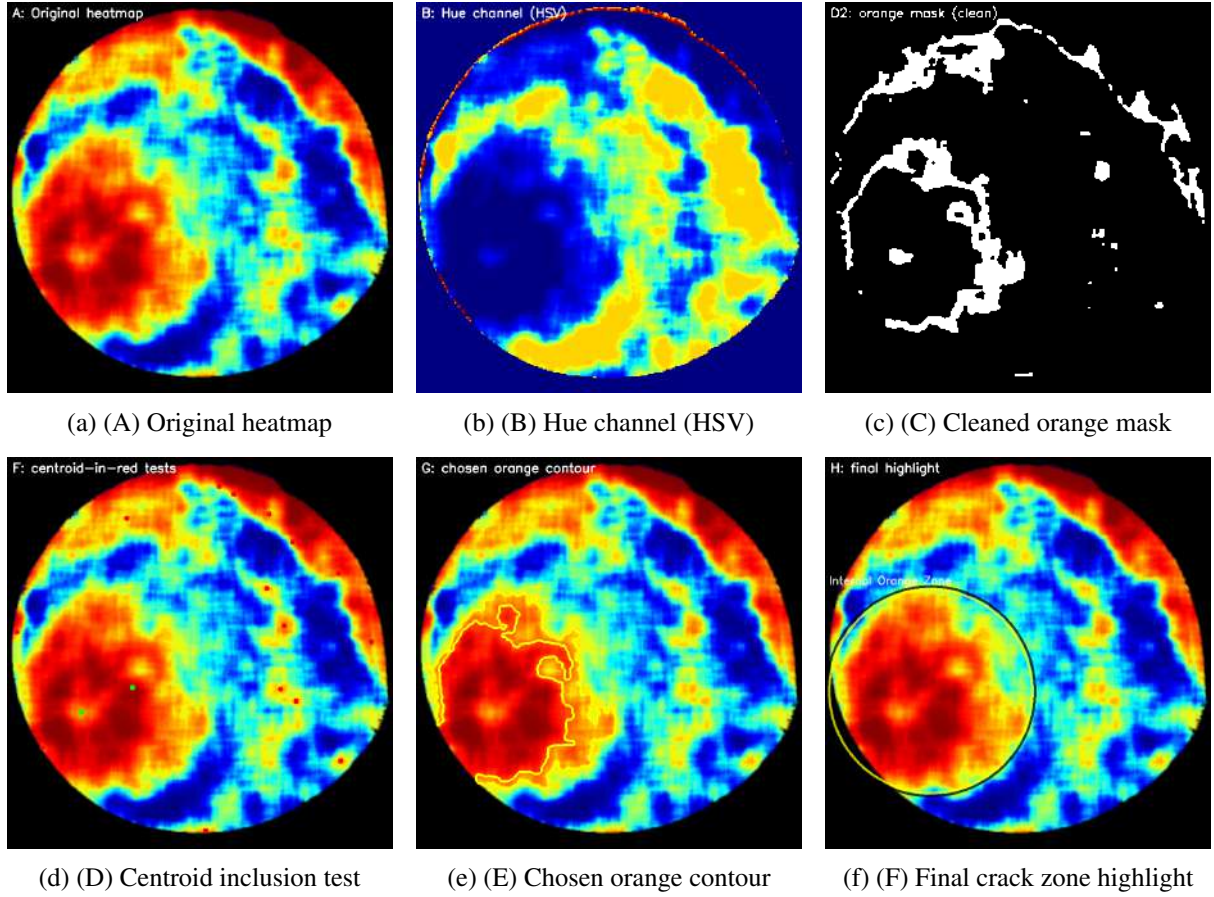


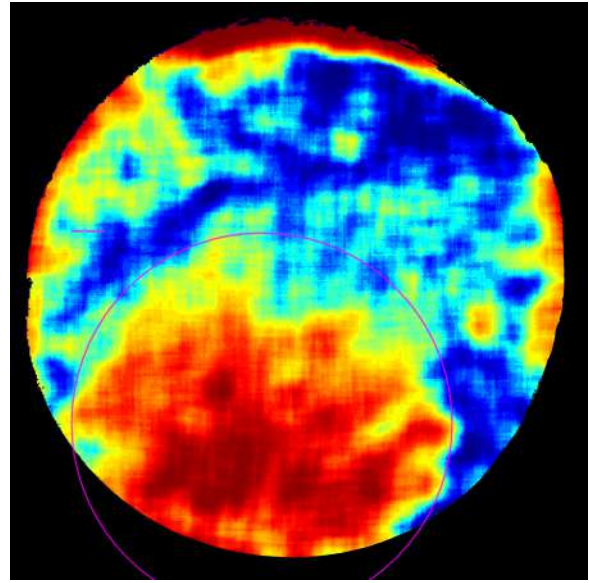
Figure 4: Stepwise crack detection process. (A) Input heatmap. (B) Hue channel separates chromatic components. (C) Morphological filtering isolates the orange high-stress region. (D) Centroid inclusion test validates orange zones inside the red boundary. (E) Largest valid orange contour is selected. (F) Final crack zone is highlighted with enclosing circle.

6.3 Visualisation for Validation

The output of the detection phase is a visual overlay on the original heatmap, designed for immediate validation. In the primary method, the selected contour is delineated using a bounding circle, calculated efficiently with the `cv2.minEnclosingCircle` function. For the alternative method, the vertices of the convex hull are used to draw a precise polygonal outline. This highlighted output serves as a final qualitative check and provides the geometric primitive that is passed on for the final stage of quantitative area and shape analysis.

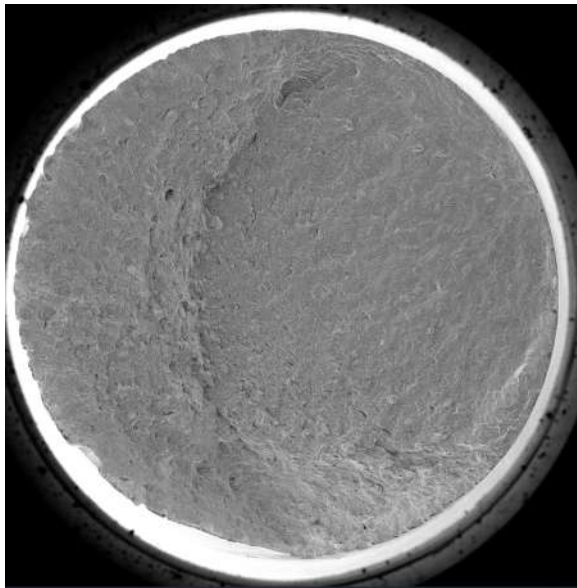


(a) Original SEM image

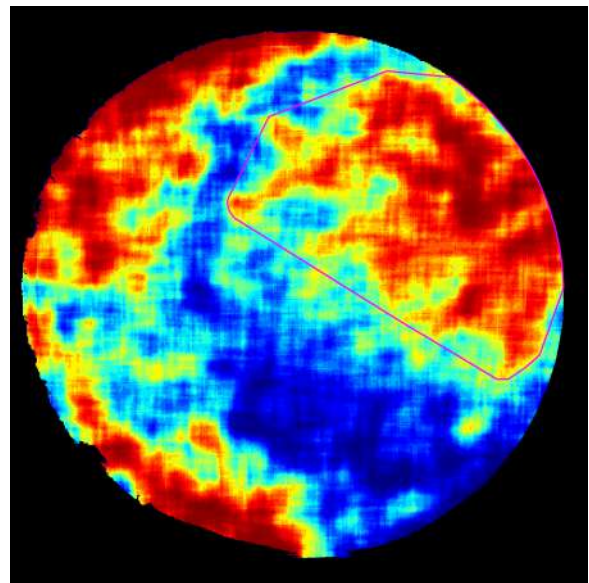


(b) Crack zone with circular overlay

Figure 5: Crack zone detection using standard method. The orange region is highlighted using the largest internal contour nested inside the red heat zone.



(a) Original SEM image



(b) Crack zone using convex hull

Figure 6: Crack zone detection using convex hull approximation. The convex polygon encloses the combined red-orange fracture region for robust highlighting in challenging cases.

6.4 Multi-Phase Contour Extraction within the Delineated Crack Zone

Following the identification and delineation of the primary crack zone, the analysis pipeline proceeds to a more granular examination of the fracture process. This next stage focuses exclusively within the boundaries of the detected crack zone to extract the precise contours of five distinct colour bands. As established in fractographic studies, different surface topographies correspond to different failure mechanisms. The heatmap was therefore segmented into areas representing these distinct phases of crack development: 'dark red' for crack initiation, 'red', 'yellow', and 'cyan' (light blue) for various stages

of stable crack propagation, and 'blue' for the final, unstable failure. By isolating and modelling each of these five phases, the methodology enables a quantitative characterisation of the entire failure sequence, a key objective in fracture mechanics.

The foundational workflow for each colour phase is executed within the spatial confines of the previously identified crack zone. This approach aligns with modern computer vision strategies for defect analysis in additively manufactured components. The heatmap is first converted to the HSV colour space (`cv2.cvtColor`), and a binary mask is generated using `cv2.inRange` with precisely calibrated HSV thresholds. This mask is subsequently refined using morphological operations (`cv2.morphologyEx`) before the phase-specific geometric analysis is performed.

6.4.1 Phase-Specific Geometric Modelling

Dark Red Phase: Crack Initiation The dark red region represents the crack initiation site, a critical phase in the fatigue life of additively manufactured alloys, which are often susceptible to process-induced defects. This phase often manifests as a cluster of small, disconnected hotspots in the heatmap. To model this, all contours within the dark red binary mask are identified, and their vertices are aggregated into a single point set. A convex hull is computed from this set using the `cv2.convexHull` function. This approach generates a single, encompassing polygon that defines the outer boundary of the entire initiation zone.

Dark Red Phase: Crack Initiation ...

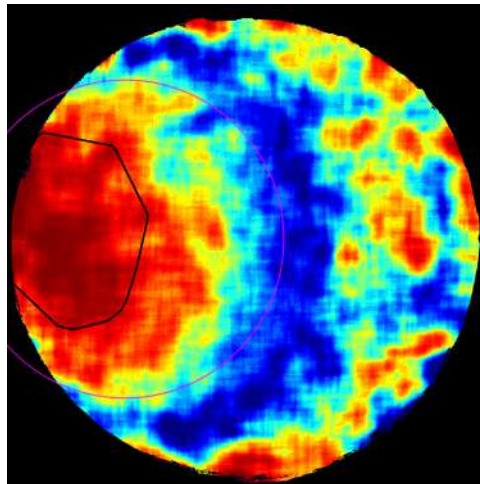


Figure 7: Detected dark red contour representing crack initiation zone.

Red Phase: Initial Crack Propagation The red region signifies the first stage of stable crack propagation, where the initial micro-cracks have coalesced into a more defined front. The analytical goal for this phase is to identify the primary, continuous boundary of this growth, which is characteristic of the fatigue process in materials like Ti-6Al-4V. This is achieved by processing the red binary mask to find all distinct contours using `cv2.findContours`. The contour with the largest area, as determined by the `cv2.contourArea` function, is selected as the definitive representation of this stage.

Red Phase: Initial Crack Propagation ...

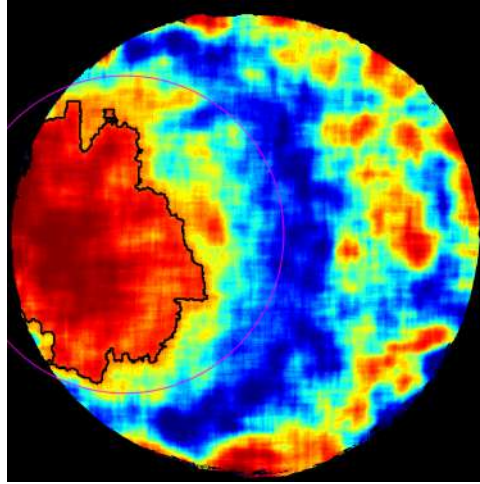


Figure 8: Detected red contour indicating stable initial crack growth.

Yellow Phase: Cumulative Fatigue Envelope The yellow band represents a further progression of stable fatigue growth. The contour for this phase is extracted by creating a cumulative binary mask that includes not only the yellow region but also all preceding warm colours. This effectively creates an "envelope" representing the total extent of the crack up to this point. From this combined mask, the largest external contour is extracted, providing a comprehensive boundary of the stable crack growth area before the transition to more rapid propagation.

Yellow Phase: Transition Zone ...

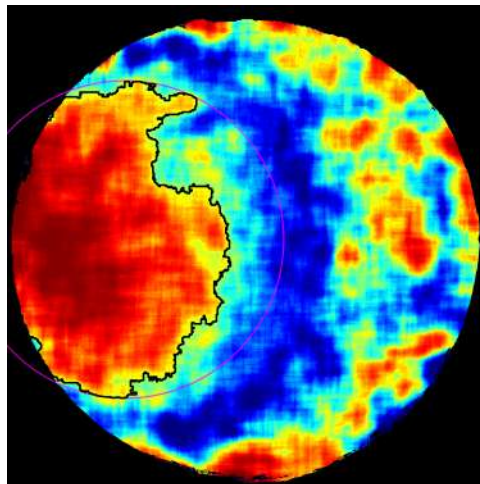


Figure 9: Detected yellow contour representing transition crack zone.

Cyan (Light Blue) Phase: Advanced Crack Propagation Front The cyan (light blue) region corresponds to a more advanced stage of stable crack propagation, representing the leading edge of the fatigue crack. The complex morphology of this front is a key feature in fractographic interpretation. To obtain a physically meaningful representation free from pixel-level jaggedness, a B-spline curve is fitted to the largest detected contour. This is accomplished using the `scipy.interpolate.splprep` and `splev` functions, which generate a smoothed, continuous mathematical curve that accurately models the intricate geometry of the crack front.

Cyan (Light Blue) Phase: Advanced Crack Propagation ...

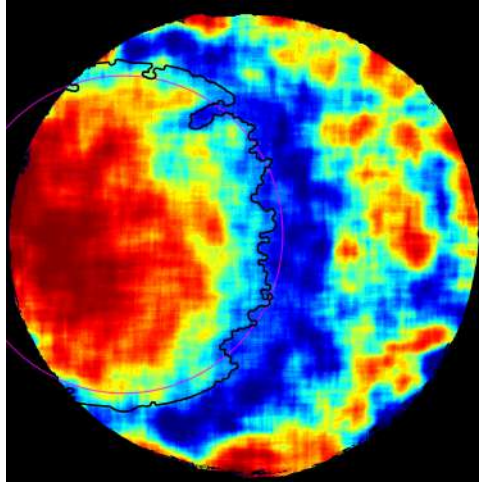


Figure 10: Detected cyan contour representing advanced crack propagation.

Blue Phase: Final Failure Envelope The blue region signifies the final failure of the specimen, where the crack transitions from stable growth to rapid, unstable fracture—a fundamental concept in fracture mechanics. For this terminal phase, the overall geometric shape and extent of the zone are more critical than the fine details of its boundary. The methodology therefore models this region by fitting an ellipse to the largest detected blue component using the `cv2.fitEllipse` function. The resulting ellipse provides a robust set of geometric descriptors that effectively characterise the final fracture event.

Blue Phase: Final Failure Envelope ...

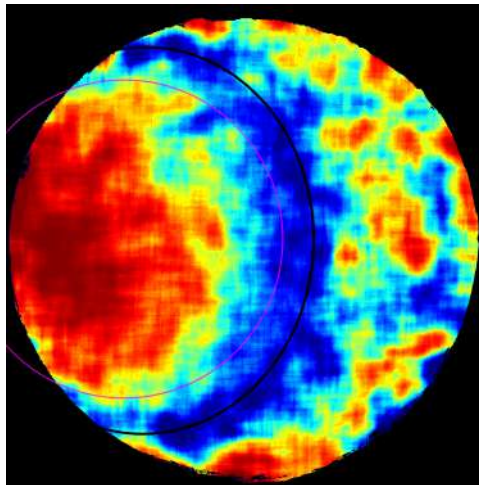


Figure 11: Detected blue contour representing the final fracture region.

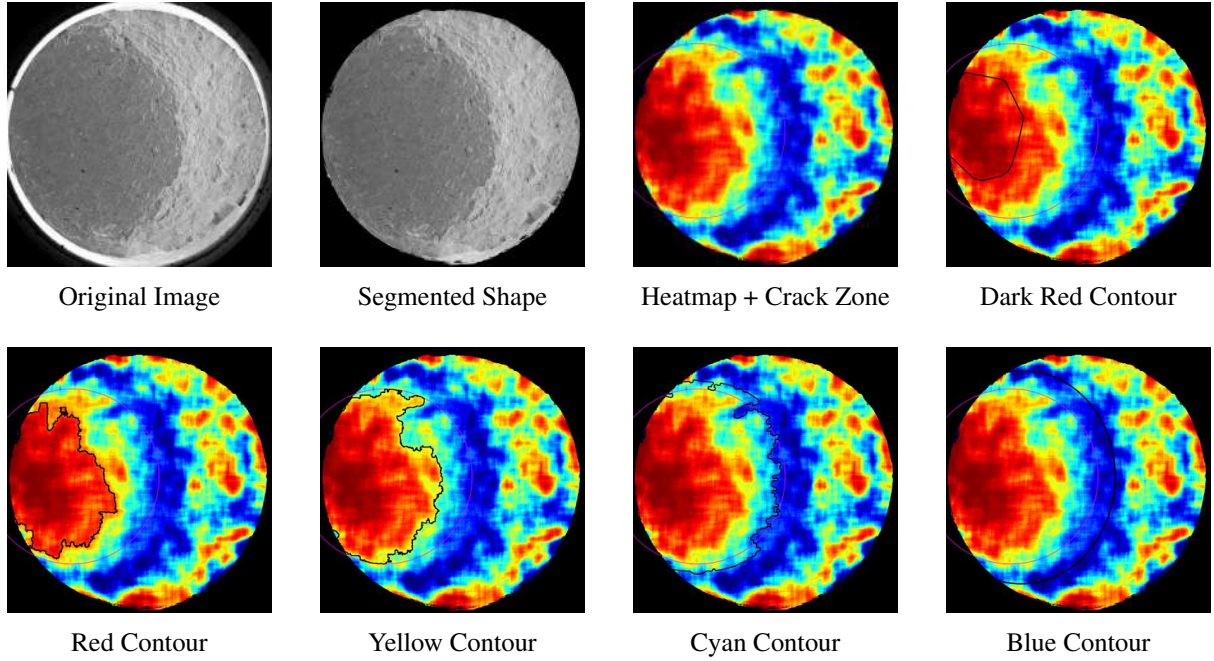


Figure 12: Step-by-step illustration of fracture analysis: original SEM image, segmentation, heatmap with crack zone, and internal contours for each crack-growth phase.

7 Quantitative Analysis and Data Reporting

The final phase of the computational pipeline transitions from geometric modelling to quantitative analysis, converting the binary masks of the crack-growth phases into a structured numerical dataset. The objective of this stage is to compute the precise area of each of the five crack-growth phases for every specimen and to report these findings in a standardised, machine-readable format. This automated reporting framework ensures objectivity and reproducibility, which are critical for enabling comparative studies in the field of fracture mechanics [1].

7.1 Area Calibration and Calculation

To ensure that all measurements are grounded in physical dimensions, a clear calibration procedure was established to convert pixel-based areas into physical units (square micrometres, μm^2). This process was based on the known resolution and field of view of the source SEM images.

Pixel Size Calibration The fundamental calibration was the determination of the physical size represented by a single pixel. Given that the SEM images have a width of 4096 pixels corresponding to a real-world field of view of 5500 μm , the linear size of each pixel was calculated as:

$$\text{Pixel Size} = \frac{5500 \mu\text{m}}{4096 \text{ pixels}} \approx 1.342773438 \mu\text{m/pixel} \quad (1)$$

This value was defined in the analysis script as the constant `PIXEL_SIZE_MICRONS`.

Micron Area Factor Assuming square pixels, the area of a single pixel in physical units is the square of its linear size. This value, termed the micron area factor, was calculated as:

$$\text{Area of one pixel} = (1.342773438 \mu\text{m})^2 \approx 1.803040504 \mu\text{m}^2 \quad (2)$$

This factor, stored in the script as the constant `MICRON_AREA_FACTOR`, represents the conversion rate from one pixel of area to its equivalent in square micrometres.

Final Area Computation The physical area of any detected crack-growth region was then computed by first counting the total number of non-zero pixels in its binary mask using `cv2.countNonZero`. This pixel count was subsequently multiplied by the `MICRON_AREA_FACTOR` to yield the final, calibrated area in μm^2 .

7.2 Data Aggregation and Structured Reporting

To ensure the data is organised for statistical analysis, the calculated areas for all five phases are systematically aggregated for each specimen using the `pandas` library to create a structured `DataFrame`. Each row corresponds to a single specimen, and the columns are constructed with a multi-level index to hierarchically organise the data into "Pixels", "micrometer²", and "scale factor" for each of the five colour-coded phases. This `DataFrame` is then exported to a Comma-Separated Values (`.csv`) file, providing a comprehensive and unambiguous record of the quantitative fractographic analysis.

7.3 Visual Validation via Contour Overlays

To complement the numerical data and provide a crucial qualitative check, the script concurrently generates visual validation overlays. For each analysed mask, the algorithm extracts the external contours using `cv2.findContours`, identifies the largest contour by area, and then draws this boundary as a thick, black line onto a copy of the original heatmap image using the `cv2.drawContours` function. These overlay images are then saved to dedicated subfolders, allowing for a direct comparison to ensure that the quantified areas accurately correspond to the visually identified features on the fracture surface.

7.4 Category-Specific Data Separation:

To enable targeted comparisons between different manufacturing routes, the pipeline generates separate CSV reports for each alloy category. For each category, the system compiles a CSV file where each row corresponds to a specimen and each column describes the internal crack-zone area for one of the five colour-coded phases (dark red, red, yellow, cyan, blue). This categorisation allows statistical analyses to be conducted independently per manufacturing method, facilitating intra-group variability analysis and inter-group comparisons.

Specimen	Dark Red	Red	Yellow	Cyan	Blue
Specimen 1	1131929	1059814	2211302	3480562	4860438
Specimen 2	706994	889925	2536824	4771324	6490205
Specimen 3	1075476	1269797	3567668	5118077	6496554
Specimen 4	1267878	1221299	2761734	4351075	7156507
Specimen 5	953945	1277775	2861131	4727964	7502239
Specimen 6	3430704	4543707	9046016	15908992	18787481
Specimen 7	1049205	1206875	2584714	3873290	5582326
Specimen 8	403552	714078	1150240	1781026	2891648
Specimen 9	699807	772311	1398250	2207186	3743580

Table 1: Area of each crack-growth phase in pixels for selected specimens

Specimen	Dark Red	Red	Yellow	Cyan	Blue
Specimen 1	2.041	1.911	3.987	6.276	8.764
Specimen 2	1.275	1.605	4.574	8.603	11.702
Specimen 3	1.939	2.289	6.433	9.228	11.714
Specimen 4	2.286	2.202	4.980	7.845	12.903
Specimen 5	1.720	2.304	5.159	8.525	13.527
Specimen 6	6.186	8.192	16.310	28.685	33.875
Specimen 7	1.892	2.176	4.660	6.984	10.065
Specimen 8	0.728	1.288	2.074	3.211	5.214
Specimen 9	1.262	1.393	2.521	3.980	6.750
AVG	1.93	2.81	7.16	12.13	15.92
STDV	1.64	2.12	6.26	11.54	12.84

Table 2: Area of each crack-growth phase in mm² for selected specimens

Interpretation of Statistical Trends. The tabulated averages (AVG) and standard deviations (STDV) across all specimens provide a concise yet informative summary of crack development behavior for each color-coded phase. The average values reflect the typical spatial extent of each phase across specimens, indicating the relative dominance of each phase in terms of fracture area. Notably, the blue and cyan phases show the largest average areas (15.92 mm² and 12.13 mm², respectively), consistent with their roles as indicators of late-stage, widespread crack propagation and final failure.

The standard deviations, on the other hand, offer critical insight into the variability and reliability of each phase across the dataset. A high STDV, such as those observed in the blue (12.84 mm²) and cyan (11.54 mm²) regions, suggests considerable diversity in how different specimens experience advanced crack growth. This can be attributed to variations in local microstructure, build orientation, or manufacturing-induced defects. Conversely, lower STDVs in the dark red and red phases indicate more consistent early crack initiation and propagation behavior across samples.

Together, these metrics allow us to assess not only the absolute extent of crack evolution but also the predictability and repeatability of these stages. Such statistical insight is essential for benchmarking the performance of different additive manufacturing methods and for informing predictive models in fracture mechanics.

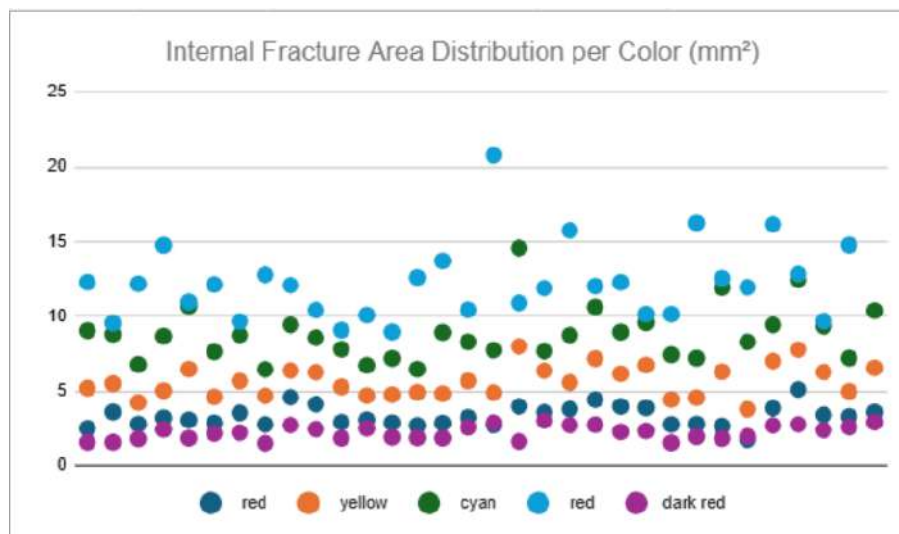


Figure 13: Internal fracture area distribution per color phase (in mm²) across all specimens. The colors represent: dark red (initiation), red (early propagation), yellow (intermediate), cyan (advanced propagation), and blue (final fracture).

8 Conclusions and Future Work

8.1 Conclusions

This work introduced an automated computer vision framework for the quantitative analysis of fracture surfaces in additively manufactured (AM) titanium and aluminum alloys. Unlike traditional fractography, which relies on subjective manual SEM inspection [16, 2], the proposed pipeline integrates multi-phase heatmap segmentation with contour-based geometric modeling to deliver reproducible and interpretable results.

Each crack stage—initiation, stable propagation, and final fracture—was automatically delineated using tailored geometric descriptors, including convex hulls, B-spline fitting, and ellipses. The resulting outputs, recorded in structured CSV files, provide calibrated area measurements in both pixel and physical units, enabling robust quantitative comparisons across specimens. This combination of interpretable geometric analysis and automated reporting aligns with recent advances in computational materials science [8, 4] and represents a significant step toward reproducible post-mortem evaluation of AM metals.

8.2 Advantages of Heatmap-Based Segmentation and Automated Quantification

The heatmap stage acts as a critical bridge between raw SEM images and quantitative fracture analysis. Raw grayscale SEM images often fail to reveal subtle transitions in crack growth due to low contrast [29, 10]. By applying gradient magnitude filtering, regional aggregation, and pseudo-color mapping, the pipeline produces standardized visualizations that enhance defect detectability and segmentation accuracy. Similar gradient-based enhancement methods have previously been applied to microstructural analysis [4, 24], confirming their utility for robust feature extraction.

The subsequent automated calculations ensure reproducibility and comparability across datasets. Manual delineation of fracture regions has long been criticized for subjectivity and inter-operator variability [16], whereas algorithmic reporting of calibrated areas enables standardized quantitative analysis. Structured numerical outputs, similar to those generated in other computer vision approaches for microstructure classification [8, 13], facilitate downstream statistical modeling, fatigue-life prediction, and cross-laboratory benchmarking.

8.3 Potential Uses and Developments

The implications of this framework span both scientific research and industrial practice. In materials research, the ability to generate large-scale, quantitative datasets of crack growth directly supports fatigue modeling efforts [11, 22]. Such datasets allow researchers to evaluate the influence of AM process parameters—including scan speed, laser power, and build orientation—on fracture behavior [5, 19]. In industrial quality control, automated defect detection has been highlighted as critical for qualifying AM parts for safety-critical aerospace and biomedical applications [26, 17]. By minimizing operator subjectivity, this method enhances reproducibility and aligns with ongoing standardization efforts.

Future developments could extend the framework in multiple directions. Hybrid approaches combining contour-based geometry with deep learning (e.g., U-Net, Mask R-CNN) have already shown promise for microstructural defect segmentation [13, 32, 18]. Expanding into three-dimensional fracture characterization via SEM stereo-photogrammetry or interferometry [30] would enable more comprehensive descriptors such as surface roughness and crack curvature. Furthermore, integrating the pipeline with in-situ monitoring systems [21, 10] could bridge the gap between real-time process control and post-mortem analysis.

Taken together, these developments could transform automated fractography from a descriptive tool into a predictive and proactive framework for materials qualification, accelerating the adoption of AM components in aerospace, biomedical, and automotive industries.

8.4 Future Work

Although the proposed framework provides a robust foundation for automated fractography, several research directions remain open for further exploration. One key avenue is the integration of deep learning into the segmentation stage. Recent work by Anidjar et al. [3] has demonstrated the potential of combining image processing with deep learning to enhance fatigue analysis of titanium alloys in additive manufacturing. Their study shows that convolutional neural networks can capture fracture morphologies with high accuracy, yet challenges related to dataset size, interpretability, and reproducibility remain unresolved. Building on these advances, future research could explore hybrid approaches that combine deep learning with the current contour-based methodology, thereby leveraging the predictive power of neural networks while maintaining geometric interpretability. Other architectures such as U-Net [13] and CNN-based classifiers [32, 18] provide further opportunities for integration.

Another promising direction involves extending the pipeline into three-dimensional characterization. Recent studies have applied SEM stereo-photogrammetry and interferometry to reconstruct fracture surface topographies in 3D [30], enabling the measurement of descriptors such as crack-front curvature and surface roughness that cannot be captured in 2D. Incorporating these methods would provide deeper insights into fatigue mechanisms in AM alloys.

The adaptation of the framework for *in-situ* or near-real-time monitoring of additive manufacturing processes is another frontier. Optical and thermal monitoring approaches have already been applied to detect porosity and lack-of-fusion defects during AM builds [10, 21]. Embedding the proposed analysis pipeline into such monitoring systems could enable proactive defect detection, bridging the gap between process control and post-mortem evaluation.

Finally, the creation of standardized benchmark datasets remains a critical step for advancing automated fractography. Previous reviews have emphasized that the lack of large, annotated datasets hampers reproducibility and cross-study comparability in AM defect detection [29, 26]. Establishing a curated repository of annotated fracture images, aligned with international qualification standards such as ISO/ASTM 52904 [17], would provide a common reference point for researchers and industry alike. Such datasets would not only validate the proposed methodology but also accelerate the development of predictive, data-driven models for AM qualification.

In summary, while the work of Anidjar et al. [3] highlights the power of deep learning for fractographic analysis, significant challenges remain unresolved. The integration of hybrid modeling, 3D fracture analysis, real-time monitoring, and standardized benchmarking represents a clear path forward. Together, these directions could transform automated fractography from a descriptive post-mortem tool into a predictive and proactive system for materials design, qualification, and deployment across aerospace, biomedical, and automotive applications.

References

- [1] T. L. Anderson. *Fracture Mechanics: Fundamentals and Applications*. 4th. CRC Press, 2017.
- [2] T. L. Anderson. *Fracture Mechanics: Fundamentals and Applications*. 4th. CRC Press, 2017.
- [3] Or Haim Anidjar et al. “Enhancing Fractographic Failure and Fatigue Analysis of Titanium Alloys in Additive Manufacturing Using Image Processing and Deep Learning”. In: *IEEE Access* 12 (2024), pp. 1–12. DOI: 10.1109/ACCESS.2024.0000000.
- [4] L. Babout and et al. “Computer vision and X-ray tomography for microstructure analysis in materials science”. In: *Materials Characterization* 147 (2019), pp. 90–108. DOI: 10.1016/j.matchar.2018.10.015.
- [5] T. DebRoy and et al. “Additive manufacturing of metallic components – Process, structure and properties”. In: *Progress in Materials Science* 92 (2018), pp. 112–224. DOI: 10.1016/j.pmatsci.2017.10.001.
- [6] T. DebRoy et al. “Additive manufacturing of metallic components – Process, structure and properties”. In: *Progress in Materials Science* 92 (2018), pp. 112–224. DOI: 10.1016/j.pmatsci.2017.10.001.
- [7] B. L. DeCost and E. A. Holm. “A computer vision approach for automated analysis and classification of microstructural image data”. In: *Computational Materials Science* 110 (2019), pp. 126–133. DOI: 10.1016/j.commatsci.2015.08.011.
- [8] B. L. DeCost and E. A. Holm. “A computer vision approach for automated analysis and classification of microstructural image data”. In: *Computational Materials Science* 110 (2019), pp. 126–133. DOI: 10.1016/j.commatsci.2015.08.011.
- [9] M. Grasso and B. M. Colosimo. “Process defects and in situ monitoring methods in metal powder bed fusion: a review”. In: *Measurement Science and Technology* 28.4 (2017), p. 044005. DOI: 10.1088/1361-6501/aa5c4f.
- [10] M. Grasso and B. M. Colosimo. “Process defects and in situ monitoring methods in metal powder bed fusion: a review”. In: *Measurement Science and Technology* 28.4 (2017), p. 044005. DOI: 10.1088/1361-6501/aa5c4f.
- [11] J. Günther and et al. “Fatigue life of additively manufactured Ti–6Al–4V in the very high cycle fatigue regime”. In: *International Journal of Fatigue* 94 (2017), pp. 236–245. DOI: 10.1016/j.ijfatigue.2016.05.017.
- [12] J. Günther et al. “Fatigue life of additively manufactured Ti–6Al–4V in the very high cycle fatigue regime”. In: *International Journal of Fatigue* 94 (2017), pp. 236–245. DOI: 10.1016/j.ijfatigue.2016.05.017.
- [13] Y. Guo and et al. “Microstructural defect segmentation in additively manufactured alloys using U-Net deep learning architecture”. In: *Additive Manufacturing* 36 (2020), p. 101552. DOI: 10.1016/j.addma.2020.101552.
- [14] Y. Guo et al. “Microstructural defect segmentation in additively manufactured alloys using U-Net deep learning architecture”. In: *Additive Manufacturing* 36 (2020), p. 101552. DOI: 10.1016/j.addma.2020.101552.
- [15] D. Hull. *Fractography: Observing, Measuring and Interpreting Fracture Surface Topography*. Cambridge University Press, 1999.
- [16] D. Hull. *Fractography: Observing, Measuring and Interpreting Fracture Surface Topography*. Cambridge University Press, 1999.
- [17] ISO/ASTM. *ISO/ASTM 52904:2021 Additive manufacturing — Process characteristics and performance — Practice for metal powder bed fusion to meet critical applications*. Standard published by ISO and ASTM International. 2021.

- [18] A. Kobler, B. Schuster, and M. Ritter. “Automated fracture surface classification using convolutional neural networks”. In: *Engineering Fracture Mechanics* 261 (2022), p. 108230. DOI: 10.1016/j.engfracmech.2022.108230.
- [19] S. Leuders and et al. “On the mechanical behaviour of titanium alloy Ti-6Al-4V manufactured by selective laser melting: Fatigue resistance and crack growth performance”. In: *International Journal of Fatigue* 48 (2013), pp. 300–307. DOI: 10.1016/j.ijfatigue.2012.11.011.
- [20] S. Leuders et al. “On the mechanical behaviour of titanium alloy Ti-6Al-4V manufactured by selective laser melting: Fatigue resistance and crack growth performance”. In: *International Journal of Fatigue* 48 (2013), pp. 300–307. DOI: 10.1016/j.ijfatigue.2012.11.011.
- [21] R. Reisch, T. Wimmer, and J. Hartmann. “In-situ monitoring of additive manufacturing using optical and thermal imaging”. In: *Additive Manufacturing* 47 (2021), p. 102280. DOI: 10.1016/j.addma.2021.102280.
- [22] S. Romano and et al. “Fatigue properties of selective laser melted Ti-6Al-4V and their relation to defect morphology”. In: *International Journal of Fatigue* 94 (2017), pp. 202–210. DOI: 10.1016/j.ijfatigue.2016.05.018.
- [23] S. Romano et al. “Fatigue properties of selective laser melted Ti-6Al-4V and their relation to defect morphology”. In: *International Journal of Fatigue* 94 (2017), pp. 202–210. DOI: 10.1016/j.ijfatigue.2016.05.018.
- [24] L. Saarimäki and et al. “Image analysis of porosity in laser additive manufactured stainless steel”. In: (2017), pp. 241–246.
- [25] L. Saarimäki et al. “Image analysis of porosity in laser additive manufactured stainless steel”. In: *Proceedings of the International Conference on Additive Manufacturing*. 2017, pp. 241–246.
- [26] M. Seifi and et al. “Overview of Materials Qualification Needs for Metal Additive Manufacturing”. In: *JOM* 69.3 (2017), pp. 439–455. DOI: 10.1007/s11837-017-2262-2.
- [27] M. Seifi et al. “Overview of Materials Qualification Needs for Metal Additive Manufacturing”. In: *JOM* 69.3 (2017), pp. 439–455. DOI: 10.1007/s11837-017-2262-2.
- [28] F. S. Silva, J. P. Oliveira, and A. M. Dias. “Image processing techniques for defect detection in additively manufactured parts: A review”. In: *Journal of Materials Processing Technology* 295 (2021), pp. 117–133. DOI: 10.1016/j.jmatprotec.2021.117133.
- [29] F. S. Silva, J. P. Oliveira, and A. M. Dias. “Image processing techniques for defect detection in additively manufactured parts: A review”. In: *Journal of Materials Processing Technology* 295 (2021), pp. 117–133. DOI: 10.1016/j.jmatprotec.2021.117133.
- [30] J. Smith, T. Brown, and L. Chen. “Three-dimensional characterization of fracture surfaces using SEM and interferometry”. In: *Materials Characterization* 197 (2023), p. 112567. DOI: 10.1016/j.matchar.2022.112567.
- [31] X. Xu et al. “Deep convolutional neural network for automatic recognition of metal fracture surfaces”. In: *Engineering Fracture Mechanics* 242 (2021), p. 107458. DOI: 10.1016/j.engfracmech.2020.107458.
- [32] X. Yang and et al. “Automatic recognition of fatigue fracture surface morphology using convolutional neural networks”. In: *Materials Science and Engineering: A* 721 (2018), pp. 1–9. DOI: 10.1016/j.msea.2018.02.010.
- [33] X. Yang et al. “Automatic recognition of fatigue fracture surface morphology using convolutional neural networks”. In: *Materials Science and Engineering: A* 721 (2018), pp. 1–9. DOI: 10.1016/j.msea.2018.02.010.